chemistry

MDPI

Article

Environmental Applications of Zeolites: Preparation and Screening of Cu-Modified Zeolites as Potential CO Sensors

Martin Jendrlin [1,*], Julien Grand [2], Louwanda Lakiss [2], Philippe Bazin [2], Svetlana Mintova [2] and Vladimir Zholobenko [1]

[1] School of Chemical and Physical Sciences, Keele University, Keele ST5 5BG, UK
[2] Laboratoire Catalyse et Spectrochimie, ENSICAEN, CNRS, Normandie Université, 6 Bd Maréchal Juin, 14000 Caen, France
* Correspondence: m.jendrlin@keele.ac.uk

Abstract: This work is focused on the application of Cu-containing zeolites as potential environmental sensors for monitoring carbon monoxide. A number of commercial zeolites with different structural properties (NaX, NaY, MOR, FER, BEA and ZSM-5) were modified using $CuSO_4$, $Cu(NO_3)_2$ and $Cu(OAc)_2$ solutions as copper sources to prepare Cu^+-containing zeolites, since Cu^+ forms stable complexes with CO at room temperature that can be monitored by infrared spectroscopy. Zeolite impregnation with $Cu(NO_3)_2$ resulted in the highest total Cu-loadings, while the $Cu(OAc)_2$-treated samples had the highest Cu^+/Cu_{total} ratio. $Cu(NO_3)_2$-impregnated MOR, which displayed the highest concentration of Cu^+, was subjected to a number of tests to evaluate its performance as a potential CO sensor. The working temperature and concentration ranges of the sensor were determined to be from 20 to 300 °C and from 10 to 10,000 ppm, respectively. The stepwise CO desorption experiments indicated that the sensor can be regenerated at 400 °C if required. Additional analyses under realistic flow conditions demonstrated that for hydrophilic zeolites, the co-adsorption of water can compromise the sensor's performance. Therefore, a hydrophobic Sn-BEA was utilised as a parent material for the preparation of an impregnated Cu-Sn-BEA zeolite, which exhibited superior resistance to interfering water while maintaining its sensing properties. Overall, the prepared Cu-modified zeolites showed promising potential as environmental CO sensors, displaying high sensitivity and selectivity under representative testing conditions.

Keywords: Cu-modified zeolites; zeolite-based sensors; CO monitoring; IR spectroscopy

Citation: Jendrlin, M.; Grand, J.; Lakiss, L.; Bazin, P.; Mintova, S.; Zholobenko, V. Environmental Applications of Zeolites: Preparation and Screening of Cu-Modified Zeolites as Potential CO Sensors. *Chemistry* **2023**, *5*, 314–333. https://doi.org/10.3390/chemistry5010024

Academic Editors: José Antonio Odriozola and Hermenegildo García

Received: 21 January 2023
Revised: 15 February 2023
Accepted: 16 February 2023
Published: 20 February 2023

1. Introduction

Carbon monoxide is a by-product of incomplete combustion of various fuels, including coal, oil and gas. The concentrations are particularly high in industries that utilise fossil fuels for power generation and in cities with high levels of traffic. CO is a colourless and odourless gas that is impossible for humans to detect. In addition, it is the leading cause of poisoning and may account for more than 50% of fatal cases reported in many industrial countries [1]. CO binds irreversibly to the iron centre of haemoglobin, the oxygen transport molecule in blood, and in that way prevents oxygen transfer throughout the organism. The maximum time-weighted average exposure value attributed by the United States National Institute of Occupational Safety and Health is 35 ppm over an 8 h period, while exposure to more than 800 ppm causes headache and dizziness, and exposure to 12,800 ppm results in death within 2–3 min [2,3]. Therefore, it is of crucial importance to monitor CO levels.

Gas sensors for environmental pollutant gases (e.g., CO) that are present on the market can be divided into two main types: optical and electronic sensors. The former can be further divided into optochemical, photoacoustic and non-dispersive infrared (NDIR) sensors. Optochemical sensors are metal salts (e.g., $PdCl_2$) that change colour upon interaction with carbon monoxide. Even though they are inexpensive, one significant

disadvantage is that the alerting system requires the vigilance of the observer to detect a change in concentration [4]. Photoacoustic spectroscopy monitors sound signals formed by the interaction of EM waves with the detector. The technique has been tested with both low and high CO concentrations, but the long signal response (~35 s) and the bulky design prevent its widespread use [5–7]. The third major type of gas sensor is the NDIR gas analyser. It shows great responses to high concentrations of CO (200–1000 ppm), but the response at lower concentrations is worse than with metal oxides [8]. Currently, most of the CO sensors on the market are based on electrochemical technology [9,10]. Electronic sensors come in two main types: thermistor-type metal-oxide-semiconductor (MOS) detectors that detect a change in heat when the target gas reacts with the oxide layer, and electrochemical detectors that work by sensing the change in charge carriers in an electrolyte solution when the target gas interacts with an electrode of the device. Sensors based on metal-oxide semiconductors (SnO_2, TiO_2, ZnO, In_2O_3) are leading in the market due to their low cost, compact design, high sensitivity and low response time [10–12].

Carbon monoxide is also a common probe molecule in the FTIR characterisation of extraframework cations, metal species and acid sites in zeolites [13]. It forms complexes with alkali, alkaline-earth and transition-metal cations at low temperatures (77 K) [14]. In the interaction with alkaline and alkaline-earth cations, mainly weak σ-bonds or electrostatic interactions are formed between the C-end of CO and the metal cation. No π-back donation can further stabilise the complex since no d-electrons are present in the outer shell [15]. However, with transition metals, both the cations themselves and the negative charge of the zeolite framework contribute to the stability of the formed complexes [16]. For practical applications of environmental CO sensors, the formation of complexes between CO and the active sites, which are stable at room temperature or higher, is required. A good example of such a stable complex is Cu^+-CO. However, copper can commonly exist as Cu^0, Cu^+ or Cu^{2+}. Due to its electron configuration, CO is preferentially adsorbed on Cu^+ ions, since both σ-bonding and π back-donation stabilise the carbonyl complex that is formed [14,15,17]. Only weak bonding is observed between CO and Cu^{2+} ions, because the σ component is not significant and no π back-donation is present. CO forms mainly a π-bond with Cu^0 atoms, but these complexes are relatively unstable and tend to dissociate below room temperature [15]. Even though a variety of Cu^+-$(CO)_x$ species have been extensively studied and characterised by FTIR, to the best of our knowledge, Cu-containing zeolites have not been utilised as sensors for CO monitoring. Therefore, in this work, we aim to introduce copper (I) species into a number of widely available zeolites with different structures and Si/Al ratios in order to obtain a functional environmental sensor operating at room temperature. In addition to impregnation and ion exchange, which are widely used, the introduction of gaseous CuCl as a Cu^+ source has been reported previously [18]. However, this procedure requires a specialised setup and high energy consumption; hence, it would not be a viable option for the mass production of potential sensors. For this reason, impregnation and ion exchange have been chosen as copper introduction methods, utilising $CuSO_4$, $Cu(NO_3)_2$ and $Cu(OAc)_2$ solutions as copper sources. The sensor materials have been systematically characterised and successfully tested for CO monitoring under representative conditions.

2. Materials and Methods

2.1. Materials

Commercial zeolites MOR (Si/Al = 10, >99%), BEA-12 (Si/Al = 12.5, >99%), BEA-19 (Si/Al = 19, >99%), ZSM-5 (Si/Al = 40, >99%), NaX (Si/Al = 1.2, >99%), NaY (Si/Al = 2.5, >99%) and FER (Si/Al = 10, >99%) were obtained from Zeolyst, Conshohocken, Pennsylvania, US. Additional background information has been provided in Table S1. Nitric acid (HNO_3, 68%), ethanol (C_2H_5OH, 70%) and acetone (C_3H_6O, >99%) were purchased from Fisher Scientific, Loughborough, UK. Copper sulphate pentahydrate ($CuSO_4 \cdot 5H_2O$, >98%), copper nitrate trihydrate ($Cu(NO_3)_2 \cdot 3H_2O$, >95%) and copper acetate monohydrate ($Cu(CH_3COO)_2 \cdot H_2O$) were purchased from Acros, Geel, Belgium. NH_4OH 35% aqueous

solution, fumed silica (SiO_2, >99%), tetraethylorthosilicate ($Si(OC_2H_5)_4$, 98%) tetraethylammonium hydroxide ($((C_2H_5)_4N(OH)$, 40%), tin (IV) chloride pentahydrate ($SnCl_4 \cdot 5H_2O$), 3-propylcellulose (M_w~80,000, >99%) and hydrofluoric acid (HF, 48%) were acquired from Sigma Aldrich, Gillingham, UK. All the materials were used as received.

2.2. Sensor Preparation

As illustrated in Figure 1, commercial zeolites were impregnated and ion-exchanged by stirring 3 g of a specific zeolite in 60 mL of the 0.1 M $CuSO_4$, $Cu(NO_3)_2$ or $Cu(CH_3COO)_2$ solutions. For the impregnated samples, after the addition of a zeolite to the solution, the pH of the initial solution (e.g., pH = 3.5 for the nitrate solution) was adjusted to pH~5–6 using a 35% NH_4OH solution in order to initiate precipitation of a basic salt and to prevent the zeolite structure degradation in acidic media. The maximum target amount of impregnated copper species on a zeolite was 2000 μmol g^{-1}. The reaction mixture was stirred vigorously for 2 h at 40 °C. Next, both the impregnated and ion-exchanged samples were centrifuged for 10 min at 5000 rpm, then decanted and washed twice with 20 mL of distilled water, followed by centrifugation and drying at 50 °C overnight.

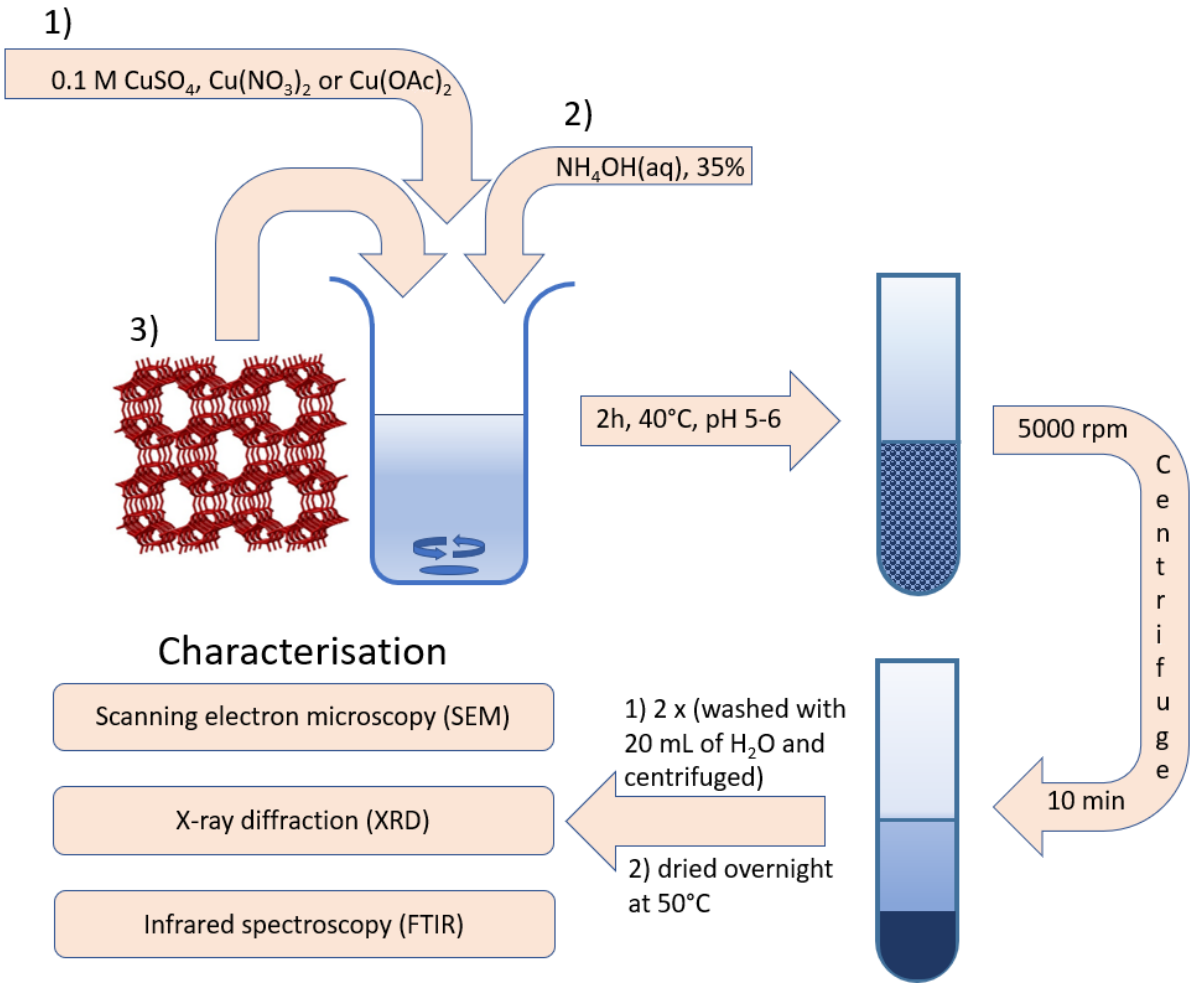

Figure 1. Cu-zeolite preparation scheme.

The hydrophobic Sn-BEA was prepared according to the procedure described in reference [19]. Briefly, 5 g of commercial BEA-19 was dealuminated in 125 mL of concentrated nitric acid for 16 h at 80 °C. Subsequently, the dealuminated sample was washed 6 times with 25 mL of deionised water and dried overnight. The material thus prepared was used as seeds in subsequent steps. The synthesis gel was prepared by mixing 6.98 g of tetraethylorthosilicate and 7.67 g of tetraethylammonium hydroxide. Subsequently, 0.12 g

of tin (IV) chloride pentahydrate was dissolved in 0.6 mL of water and added dropwise to the gel. The Si/Sn molar ratio in the gel was 100. The gel was stirred for 12 h in a closed container and then for 3 days in an open container. After allowing the excess water and ethanol to evaporate, 0.74 g of hydrofluoric acid was added to the gel. Next, 0.085 g of seeds suspended in 0.58 g of water was added to a homogenised gel and mixed thoroughly. The mixture was heated for 6 days at 140 °C in an autoclave. The solid product was isolated and washed 5 times with 25 mL of water, followed by 5 washes with 25 mL of acetone. Finally, the sample was dried overnight.

Sensors were made according to a previously described procedure [20]. Silicon wafers were cut into 10 × 10 mm squares and cleaned with ethanol and acetone. The as-prepared sample was dispersed in acetone (4 wt%), mixed with 3-propylcelulose as a surfactant and deposited in several layers as a thin film on silicon wafers (10 × 10 mm) by spin coating (Laurell spin coater, Horsham, PA, USA, model WS-400B-6NPP-LITE). The prepared films were then calcined for 30 min at 450 °C (ramp rate 5 °C min^{-1}).

2.3. Sensor Characterisation

Zeolite samples were characterised by using scanning electron microscopy (SEM) (Hitachi TM 3000, London, UK, with Bruker EDX, Durham, UK (energy-dispersive X-ray analysis) analytical system at 500× magnification, 300s EDX exposition time), X-ray powder diffraction (XRD) (Bruker D8 Advance diffractometer, Durham, UK, Cu Kα at 40 kV and 40 mA, 2θ = 5−60°), in situ XRD experiments (Bruker D8 Advance, Durham, UK, Cu Kα at 40 kV and 40 mA, 2θ = 5−60°, ramp 1 °C min^{-1} to 450 °C, pattern collected at 200 °C), thermogravimetric analysis (TGA) (Rheometric Scientific STA, 1500, 20–800 °C, 10 °C min^{-1}, 40 mL min^{-1} N_2 flow), N_2 adsorption-desorption (Quantachrom iQ Autosorb instrument, St. Albans, UK), TEM (FEI Tecnai G2 30 UT LaB_6 microscope, Columbus, Ohio, US, more details in [21]) and Fourier-transform infrared spectroscopy (FTIR) (Thermo iS10 spectrometer, Loughborough, UK, with a custom-made vacuum cell, 6000−1000 cm^{-1}, 64 scans, 4 cm^{-1} resolution, transmission mode).

Prior to collecting the SEM micrographs and EDX analysis, samples were mounted onto aluminium holders, fixed with carbon cement and carbon-coated. The magnification was 500×, which provided an observation area of ~300 × 300 μm. The samples had to be carbon-coated; hence, carbon percentage was excluded from elemental analysis, which only affected the analysis of copper-acetate-treated samples. Elements of interest were silicon, aluminium and copper for all the samples, and sulphur or nitrogen for the sulphate- and nitrate-based samples, respectively.

Prior to FTIR analysis, samples were also pressed into pellets (13 mm diameter, 10−15 mg), activated in a vacuum cell (Figure S1 in Supplementary Materials) by heating to 450 °C (ramp 1 °C min^{-1}), kept for 5 h at 450 °C, then cooled to 30 °C under vacuum, after which the IR spectra were collected. In a preliminary test, 1 mbar of CO was introduced into the cell at 30 °C, the IR spectrum of the sample was collected in the CO atmosphere, the sample was evacuated for 10 min, and another spectrum was collected. In the titration experiment, a portion of 2 μmol of CO was added to the cell before collecting each spectrum.

2.4. Operando Gas Detection

Experiments testing the sensor's performance were conducted using a custom-made operando cell in a flow system with argon containing 100 ppm of water as the carrier gas. Prior to the controlled adsorption of CO (10 to 10,000 ppm of CO in Ar), the samples were activated in situ at 250 °C for 30 min (ramp rate 3 °C min^{-1}) and cooled down to ambient temperature. The FTIR spectra were collected using a Thermo iS50 spectrometer equipped with an MCT detector, using 64 scans at 4 cm^{-1} resolution in the 6000−1000 cm^{-1} spectral range. All the sensor performance data presented are the difference spectra obtained by subtraction of the zeolite spectrum prior to the gas adsorption experiment from the spectrum of a sample at a specific concentration of the target gas. Since water vapour was inherently present in the argon flow, gas-phase water correction was applied. For all

waterfall data sets, the spectra are offset for clarity, and the colour legend represents the absorbance scale.

3. Results and Discussion

To prepare the optimal zeolite-based CO sensor for environmental applications, a screening of a variety of commercially available zeolites was undertaken. The selected zeolites were chosen because of their wide range of Si/Al ratios (Si/Al = 1.3–40), pore width (5.0–7.4 Å), channel networks (1D to 3D) and crystallite sizes (0.04–0.80 µm) (see Table S1 [22]). All the commercial materials were characterised by BET, XRD, TGA and FTIR (Figures S18–SC46, Table S2 (Supplementary Characterization file)).

3.1. SEM-EDX

Initially, both copper introduction methods were compared in a model system using MOR and the $Cu(NO_3)_2$ solution. From Table 1, it can be concluded that the copper loading for the MOR impregnated by $Cu(NO_3)_2$ (MOR-$Cu(NO_3)_2$) was more than five times greater than that for the ion-exchanged zeolite. Since a higher copper loading should lead to a higher sensitivity of the sensor towards CO, impregnation was chosen as a method for screening the sensing performance of other zeolites. Additionally, the increasing Si/Al ratio of the ion-exchanged sample is indicative of the potential degradation of the zeolite frameworks during ion-exchange using solutions with pH < 7.

Table 1. EDX characterisation data of Cu-impregnated samples (* ion-exchanged sample).

Zeolite	Si (at.%)	Al (at.%)	Cu (at.%)	Si/Al	Cu/Al
MOR-$CuSO_4$	76.6	8.2	12.6	9.3	1.5
MOR-$Cu(NO_3)_2$	78.4	8.4	13.2	9.4	1.6
MOR-$Cu(OAc)_2$	80.5	8.1	11.4	9.9	1.4
MOR-$Cu(NO_3)_2$-IE *	89.4	8.3	2.3	10.7	0.3
BEA-12-$CuSO_4$	78.8	6.3	11.6	12.5	1.8
BEA-12-$Cu(NO_3)_2$	63.7	5.2	13.5	12.2	2.6
BEA-12-$Cu(OAc)_2$	84.2	6.6	9.2	12.8	1.4
BEA-19-$CuSO_4$	80.1	4.2	12.5	19.0	3.0
BEA-19-$Cu(NO_3)_2$	80.0	4.5	15.5	17.9	3.5
BEA-19-$Cu(OAc)_2$	87.2	4.5	8.4	19.5	1.9
ZSM-5-$CuSO_4$	84.1	2.4	10.8	35.2	4.5
ZSM-5-$Cu(NO_3)_2$	68.5	2.0	13.4	33.7	6.6
ZSM-5-$Cu(OAc)_2$	87.1	2.4	10.5	36.1	4.4
NaX-$CuSO_4$	39.9	30.4	11.7	1.3	0.4
NaX-$Cu(NO_3)_2$	42.1	31.6	11.0	1.3	0.4
NaX-$Cu(OAc)_2$	44.9	31.7	8.6	1.4	0.3
NaY-$CuSO_4$	54.5	20.3	12.6	2.7	0.6
NaY-$Cu(NO_3)_2$	55.4	20.4	15.3	2.7	0.7
NaY-$Cu(OAc)_2$	59.9	21.6	9.1	2.8	0.4
FER-$CuSO_4$	81.3	8.4	8.2	9.7	1.0
FER-$Cu(NO_3)_2$	74.3	7.4	11.4	10.1	1.5
FER-$Cu(OAc)_2$	82.6	8.7	8.8	9.5	1.0

It should be noted that the observed Si/Al ratios of the zeolites in Table 1 are close to those listed in the product specifications of the parent zeolites, which is indicative of zeolite framework preservation during the impregnation process. Copper loadings showed a trend in which samples from acetate solutions had the lowest value, followed by sulphate and nitrate. In most cases, the difference between the highest and lowest value for each zeolite was ~3 at%, but in the case of BEA-19, the difference was the highest (~7 at%).

3.2. XRD

As mentioned above, impregnation methods were used to introduce copper into the zeolites since ion-exchanged samples had a significantly lower Cu-loading. In this

work, the difference between the two copper introduction methods was in the pH of an exchange solution. When the pH depended only on the initial solution of the copper salt, ion exchange occurred. If the pH of a solution was adjusted, no ammonia complexes were detected; only the basic analogues of the initial copper salts precipitated (Figure S2). For example, from the $Cu(NO_3)_2$ solution, $Cu_2(NO_3)(OH)_3$ precipitated, which is present in nature in two polymorphic forms as minerals: gerhardtite (orthorhombic) and rouaite (monoclinic). In these reaction conditions, only the monoclinic form was detected. The XRD patterns of the precipitated salts were compared to the calculated patterns from the Inorganic Chemical Structural Database (ICSD) and International Centre for Diffraction Data (ICDD) databases (Figure S2a). From the $CuSO_4$ solution, several basic salts could precipitate, but only $CuSO_4 \cdot 3Cu(OH)_2$, known as brochantite, was observed (Figure S2b). In the case of the $Cu(OAc)_2$ solution, $[Cu(OAc)_2]_2 \cdot Cu(OH)_2 \cdot 5H_2O$, which is known as the blue-green pigment verdigris (Figure S2c), precipitated. The presence of the basic salts in the case of MOR-$Cu(NO_3)_2$ was detected by comparing the XRD patterns of the parent and impregnated zeolites before the high-temperature activation (Figure 2). XRD patterns of MOR and MOR-$Cu(NO_3)_2$ were collected from the experimental samples, while the XRD pattern of $Cu_2(NO_3)(OH)_3$ was calculated from the structure deposited in ICSD. In the MOR-$Cu(NO_3)_2$ pattern, four additional peaks can be noticed (2Θ = 12.8°, 32.0°, 33.5° and 36.4°) that do not appear in the parent MOR pattern; they correspond to the peaks from the calculated $Cu_2(NO_3)(OH)_3$ pattern. Therefore, it can be concluded that the new phase is present in the copper-impregnated sample.

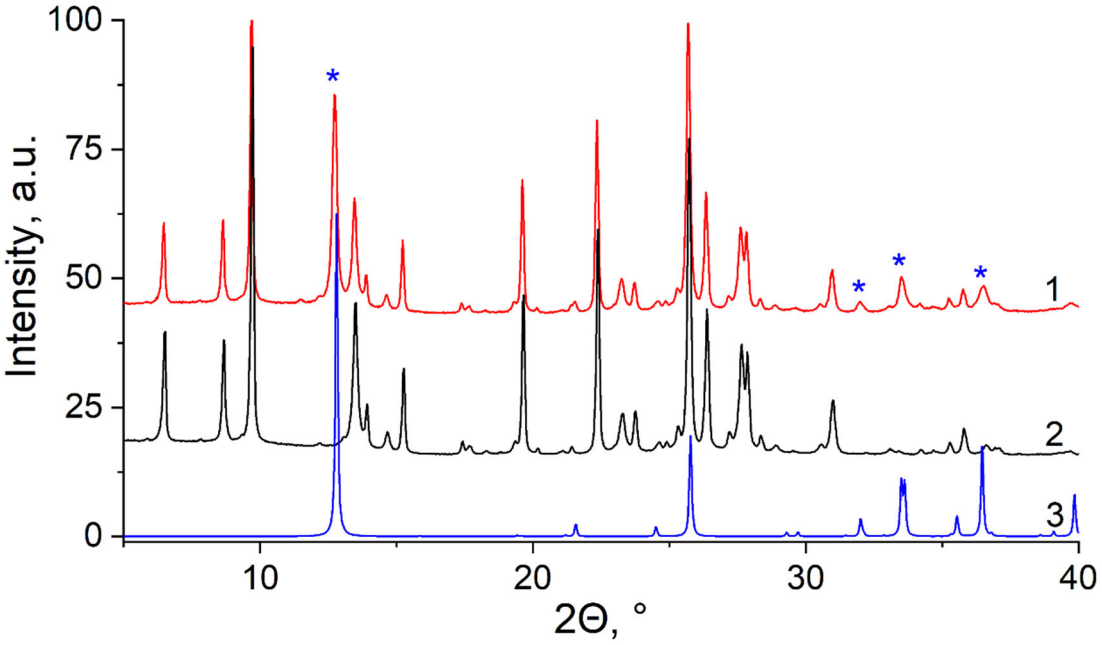

Figure 2. XRD patterns of Cu-MOR before activation (1), MOR (2), and $Cu_2(NO_3)(OH)_3$ before activation (3); patterns are offset for clarity, and peaks corresponding to phase (3) are marked with blue asterisks.

Prior to in situ characterisation, the samples were pressed into pellets (m = 10−15 mg) and activated under vacuum at 450 °C for 5 h, leading to the removal of adsorbed water and a partial reduction from Cu^{2+} to Cu^{+} [14,18,23]. After the activation process, the pellets changed colour from a distinctive blue-green to black. This was an indication that the portion of Cu-complexes adsorbed on the zeolite surface transformed into copper (II) oxide (Figure 3). This was confirmed by the in situ XRD experiment simulating the activation conditions. The vacuum conditions during the activation process were simulated by the flow of N_2 as an inert gas. Before the activation, the $Cu_2(NO_3)(OH)_3$ phase was present. Its

peaks (2Θ = 12.8°, 32.0°, 33.5° and 36.4°) disappeared after the activation, and new peaks corresponding to copper (II) oxide appeared (2Θ = 29.5°, 32.5°, 35.5° and 38.8°), while no copper (I) oxide peaks were observed (Figure S3).

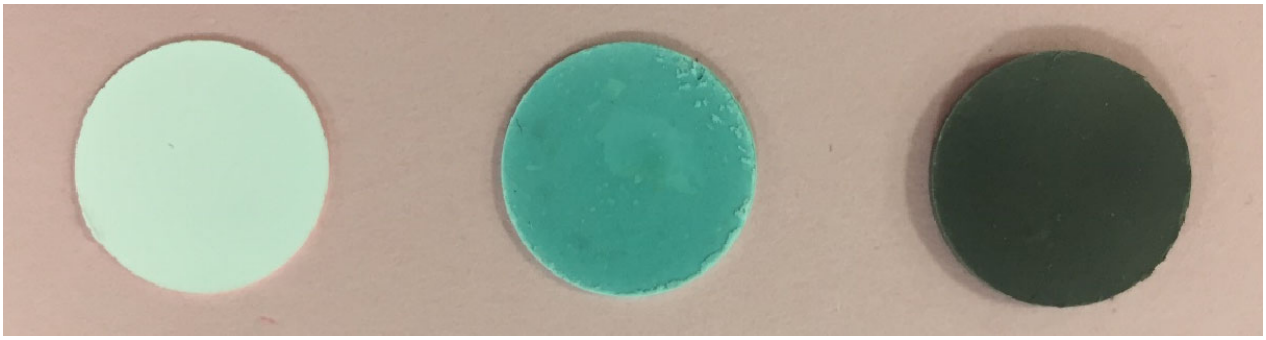

Figure 3. Zeolite samples pressed into pellets: parent zeolite MOR (**left**), MOR-Cu$(NO_3)_2$ before activation (**middle**), and MOR-Cu$(NO_3)_2$ after activation (**right**).

3.3. FTIR

During FTIR characterisation, the area of interest was 2000–2200 cm^{-1}, where the characteristic bands of Cu···CO complexes appear. Absorption peaks of gaseous CO were observed between 2171 and 2120 cm^{-1} (Figure S4), while the bands representing Cu^+-CO interaction within the zeolite framework were observed from 2150 to 2160 cm^{-1} (Table 2). Apart from the main Cu^+-CO band, the Cu^+-$(CO)_2$ and Cu^+-$(CO)_3$ bands have also been described. [14,15]. During the CO adsorption-desorption measurements performed in this research, the most intense band was detected at ~2155 cm^{-1}, corresponding to the C≡O stretching vibration of the Cu^+-CO complex, while bands at ~2125 and 2177 cm^{-1}, which can be assigned to Cu^+-$(CO)_2$ symmetric and antisymmetric stretching, respectively [14,17], appeared as shoulders.

Table 2. FTIR bands of CO adsorbed on Cu-impregnated zeolites (* data obtained in this work).

Zeolite	Cu^+-CO *, cm^{-1}	Cu^+-$(CO)_2$ *, cm^{-1}	Cu^+-CO, cm^{-1}	Cu^+-$(CO)_2$, cm^{-1}
NaX	2153	2176, 2113	-	-
NaY	2148	2157, 2108	2143 [24]	2168, 2135 [24]
MOR	2156	2178, 2108	2159 [25]	2180, 2152 [25]
FER	2155	2177, 2115	2157 [26]	2178, 2142 [26]
BEA-12	2154	2180, 2130	2157 [24] 2158 [27]	2180, 2152 [24] 2180, 2152 [27]
BEA-19	2157	2179, 2132	-	-
ZSM-5	2156	2176, 2133	2158 [24] 2157 [28]	2178, 2150 [24] 2178, 2151 [28]

Since Cu^{2+} and Cu^0 interactions with CO are too weak to be detectable at room temperature, all the observed IR bands can be assigned to Cu^+-CO. Zeolites are an essential component of a Cu^+-based sensor, since basic copper salts impregnated on non-zeolitic systems such as silica have shown no response towards CO at room temperature (Figure S4). Zeolite structure favours the formation of Cu^+ cations by having dispersed cationic sites and smaller cages that would stabilise isolated Cu^+ species [14]. Additionally, the presence of Brønsted acid sites within the framework can contribute to the controlled reduction of Cu^{2+} to Cu^+ rather than the complete reduction to Cu^0.

The reduction of Cu^{2+} to Cu^+ was observed within the zeolite channels of MOR modified by Cu$(NO_3)_2$ via ion exchange or impregnation. Both samples showed similar peak shapes and positions, but the total peak area was 3–5 times higher for the impregnated sample (Figure S5). This ratio was lower than the copper loading ratio determined by

EDX, which can be explained by the distribution of Cu species within the zeolites that are not completely dispersed as isolated Cu^+ ions but exist along with Cu(0) and Cu(II) [17]. Indeed, bulk CuO was observed both visually and in the XRD patterns (Figures 3 and S3). The number of Cu^+ sites interacting with CO was also dependent on the copper source utilised for the impregnation of the zeolite (e.g., BEA-12) (Figure S6).

Theoretical calculations have shown that the Cu^+-CO interaction depends not only on the position of copper ions but also on the surrounding framework [16]. The FTIR spectra collected in this work are in agreement with these findings, indicating that the positions and relative intensities of the peaks vary for different zeolite frameworks (Figure 4).

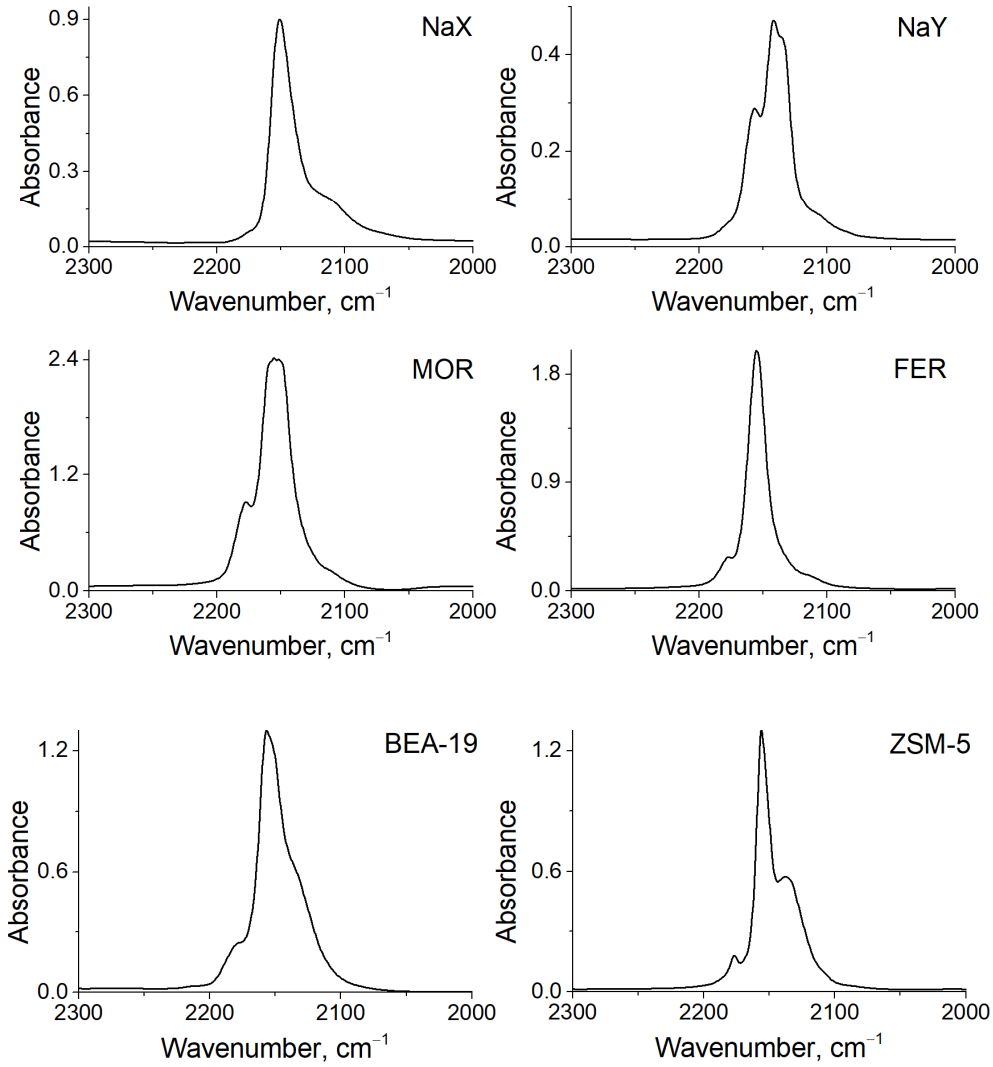

Figure 4. Difference FTIR spectra of CO adsorbed on $Cu(NO_3)_2$-impregnated zeolites.

From the measured peak area, the total amount of adsorbed CO can be calculated using the Beer–Lambert law [29]:

$$n(CO) = \frac{A(peak) \cdot S(sample)}{\varepsilon(peak) \cdot m(sample)} \quad (1)$$

where ε is the molar extinction coefficient [cm μmol^{-1}] of Cu^+-CO [15], A is the peak area [cm^{-1}], S is the sample disc cross-section [cm^2], m is the sample mass [g] and n is the amount of CO per gram of the sample [μmol g^{-1}]. The data for all the used zeolites are summarised in Table 3. Even though the observed peaks are a combination of bands

representing stretching vibrations of both the Cu^+-CO and Cu^+-$(CO)_2$ species, the total area of the peaks was utilised since only the molar extinction coefficient of the Cu^+-CO band has been published [15]. Bearing in mind the most likely sensor design, which would make use of non-dispersive infrared (NDIR) technology with its relatively low spectral resolution, this approximation seems satisfactory. Assuming that the Cu^+-CO complexes are the major species present, the calculated amount of CO equals the amount of Cu^+ in the sample (Table 3). These data confirm that not all copper in the samples is present as Cu^+ and that, due to various redox reactions, e.g., autoreduction and disproportionation, different species containing Cu(II) and Cu(0) are formed [17]. From the total amount of copper in the sample, only the fraction represented by the Cu^+ species is utilised for the detection and sensing of CO, which could be optimised either by controlled reduction during activation or by impregnation using different copper sources.

Table 3. CO adsorption-desorption FTIR data, scaled to 10 mg, (ε = 13.5 cm μmol^{-1} [15]).

Zeolite	Area CO	µmol CO/g of Zeolite #	µmol Cu/g of Zeolite, Total †	Cu^+/Cu **
MOR-$CuSO_4$	74.3	672	1227	0.55
MOR-$Cu(NO_3)_2$	88.7	801	1101	0.73
MOR-$Cu(OAc)_2$	60.8	549	899	0.61
MOR-$Cu(NO_3)_2$ *	26.2	237	229	1.03
BEA-12-$CuSO_4$	18.1	164	1545	0.11
BEA-12-$Cu(NO_3)_2$	40.9	370	1279	0.29
BEA-12-$Cu(OAc)_2$	54.7	495	1192	0.42
BEA-19-$CuSO_4$	20.1	181	1190	0.15
BEA-19-$Cu(NO_3)_2$	46.1	417	1126	0.37
BEA-19-$Cu(OAc)_2$	69.5	628	735	0.86
ZSM-5-$CuSO_4$	11.3	102	1498	0.07
ZSM-5-$Cu(NO_3)_2$	34.0	307	1315	0.23
ZSM-5-$Cu(OAc)_2$	32.3	292	797	0.37
NaX-$CuSO_4$	16.4	148	1173	0.13
NaX-$Cu(NO_3)_2$	26.1	236	1096	0.21
NaX-$Cu(OAc)_2$	47.8	432	858	0.50
NaY-$CuSO_4$	5.8	52	1228	0.04
NaY-$Cu(NO_3)_2$	16.0	144	1432	0.10
NaY-$Cu(OAc)_2$	13.4	121	829	0.15
FER-$CuSO_4$	29.3	265	820	0.32
FER-$Cu(NO_3)_2$	46.7	422	1135	0.37
FER-$Cu(OAc)_2$	44.5	402	877	0.46

(* Ion-exchanged sample; ** $n(CO) \approx n(Cu^+)$; # determined by FTIR; † determined by EDX).

It can be concluded from the data that the highest Cu^+/Cu ratio was observed in the ion-exchanged MOR sample. However, in terms of total amount of Cu^+ sites, the impregnated counterpart has more than three times as much Cu^+ interacting with CO. Across the series, impregnated samples contained between 735 and 1545 µmol of Cu per gram of zeolite. Considering the data presented in Table 3, the greatest Cu^+/Cu ratios were achieved for the copper acetate-treated samples, whereas the copper nitrate-impregnated samples showed a higher total amount of Cu in the sample. Indeed, BEA-19-$Cu(NO_3)_2$ showed the highest percentage of copper (I), and the sample with the highest value of the total copper present in the sample was MOR-$Cu(NO_3)_2$. In general, the faujasite samples showed the lowest amount of total Cu and Cu^+, whereas the MOR- and BEA-based samples showed the highest values. Several factors could contribute to these results, e.g., Si/Al ratio, channel network and pore size. In zeolites such as NaX and NaY, with Si/Al ratios of ~1.3 and 2.6, respectively, ion-exchange with doubly charged cations was favoured because the aluminium sites, and thus the negative charges, were in greater proximity compared to the zeolites with a high Si/Al ratio. For the zeolites with a higher Si/Al ratio, the lower charge density should favour the existence of Cu^+ species. However, the higher the Si/Al ratio, the lower the number of possible exchange sites for Cu^+ cations.

The Cu^+ concentration in ZSM-5 (Si/Al = 40) was among the lowest, most likely due to the lower total number of possible Cu^+ sites. It could be concluded that the optimal Si/Al ratio was ~10–20, since MOR and BEA-19 showed the best Cu^+/Cu ratios among the impregnated samples. Additionally, it was found that most of the Cu^+ species in MOR were stabilised in the side pockets of the main channel and, therefore, were less likely to undergo disproportionation or autoreduction [14]. This was confirmed by comparison with FER, which had the same Si/Al ratio but a different type of framework. In general, a higher Cu^+/Cu ratio was observed for the MOR, BEA and ZSM-5 zeolites compared to NaX and NaY. This could be explained by the fact that the larger pore size and the high Al concentration in faujasites facilitate the formation of copper (II) species and larger nanoparticles within the zeolite [17]. Therefore, subsequent research was focused on MOR and BEA-19.

3.4. CO Titration and Stepwise Desorption at Different Temperatures on MOR-Cu(NO_3)$_2$

The MOR-Cu(NO_3)$_2$ sample was subjected to a titration experiment at room temperature (Figure 5a,c) to determine if it was possible to discriminate different concentrations of CO.

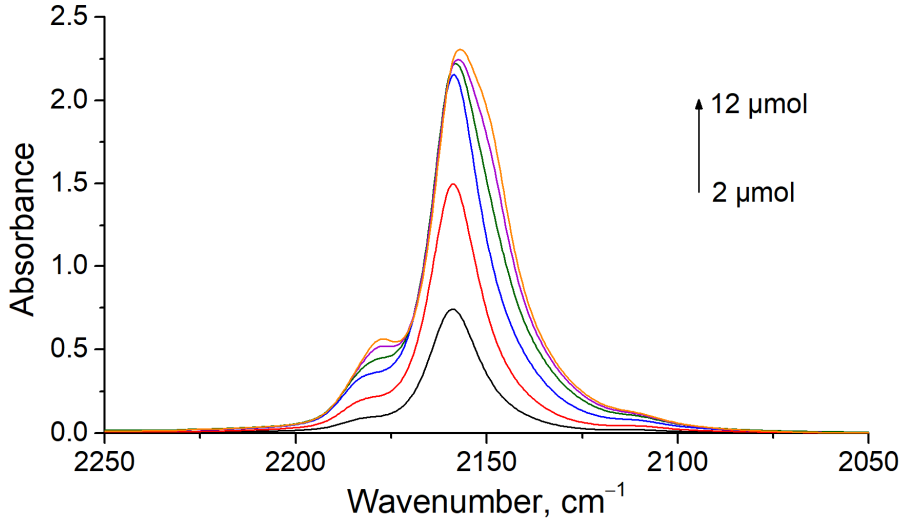

(**A**)

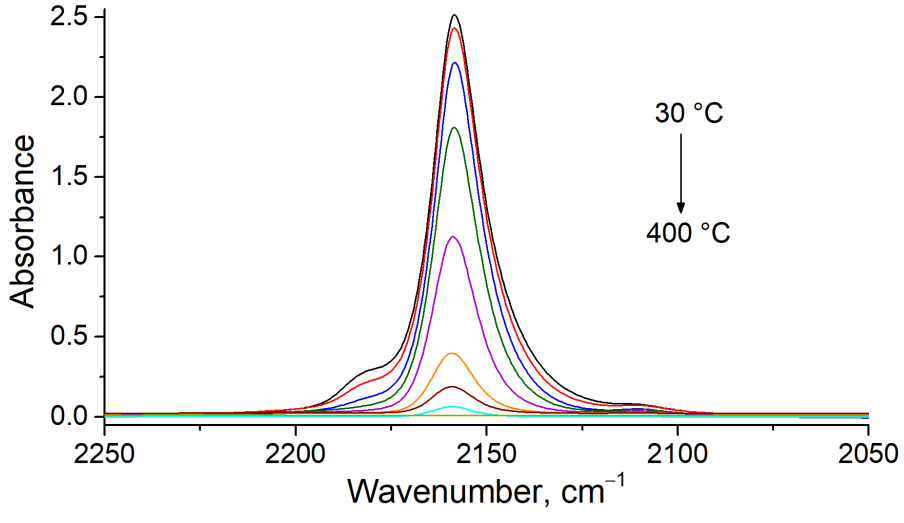

(**B**)

Figure 5. *Cont.*

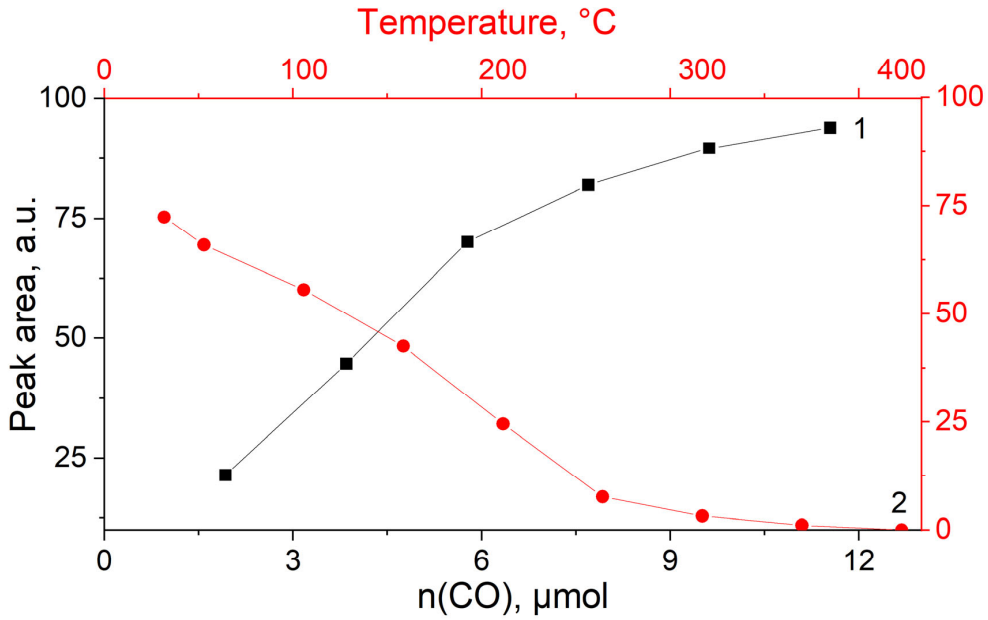

(**C**)

Figure 5. (**A**) Difference FTIR spectra of CO adsorbed on MOR-Cu$(NO_3)_2$. CO titration experiment with increments of ~2 μmol of CO. (**B**) Stepwise desorption at different temperatures; difference FTIR spectra of CO adsorbed on Cu$(NO_3)_2$-impregnated MOR. (**C**) Evolution of the IR peak area following CO adsorption on MOR-Cu$(NO_3)_2$ (1), and evolution of IR peak area during stepwise desorption at different temperatures of CO on MOR-Cu$(NO_3)_2$ (2).

In this experiment, the pelletised sample was titrated with doses of 8 mbar of CO from a 6 mL container (2 μmol) at room temperature. Initially, only the 2159 cm^{-1} peak was present, but at higher concentrations, shoulders at 2177 and 2150 cm^{-1} developed, which could be attributed to Cu^+-$(CO)_2$ stretching vibrations. At the highest CO partial pressure, the shoulder at 2150 cm^{-1} became the most intense. In addition, stepwise desorption at different temperatures was conducted (Figure 5b) to determine the regeneration temperature of a sensor. After 30 min at 30 °C, the peak area decreased (Figure S7). The decrease in intensity was mainly due to the loss of $Cu^+(CO)_2$ species upon evacuation at 30 °C. Since the Cu^+-CO interaction is strong, a desorption temperature of 400 °C was required to remove all of the CO from the sample, indicating that the sensor could be utilised at temperatures up to 400 °C.

All the previous experiments were conducted in a controlled atmosphere in a vacuum system, but to simulate the working conditions of a sensor, an atmospheric test was undertaken. In this experiment, the sensor was exposed to ambient atmospheric conditions after the standard activation procedure. Following that, the spectrum of the blank sample was collected, and the sample was exposed to ~100 ppm of CO in air. Even though the bands at 1640 cm^{-1} and 2500–3700 cm^{-1}, attributed to water adsorbed on the zeolite, were the most significant, the peak corresponding to the Cu^+-CO (2159 cm^{-1}) interaction could still be observed (Figure S8). However, this experiment indicates that atmospheric water would significantly disturb the operational performance of a sensor.

3.5. In Situ CO Adsorption on Cu$(NO_3)_2$-Impregnated MOR

In the in situ experiments, a MOR-Cu$(NO_3)_2$ sample was deposited on a Si wafer and tested using a flow system (15–900 ppm of CO in an Ar atmosphere and 100 ppm of H_2O; see Figures 6A,B and S9). Interestingly, the peak corresponding to the Cu^+-CO shifted from 2157 cm^{-1} to 2135 cm^{-1} at higher CO concentrations. This transition can be attributed to the presence of water vapour in the test gases, as reported previously [15]. It should be noted that a strong IR signal was observed at the lowest CO concentration (15 ppm). The

total peak area then increased with the increasing CO concentration, reaching a plateau at ~200 ppm of CO (Figure 6B).

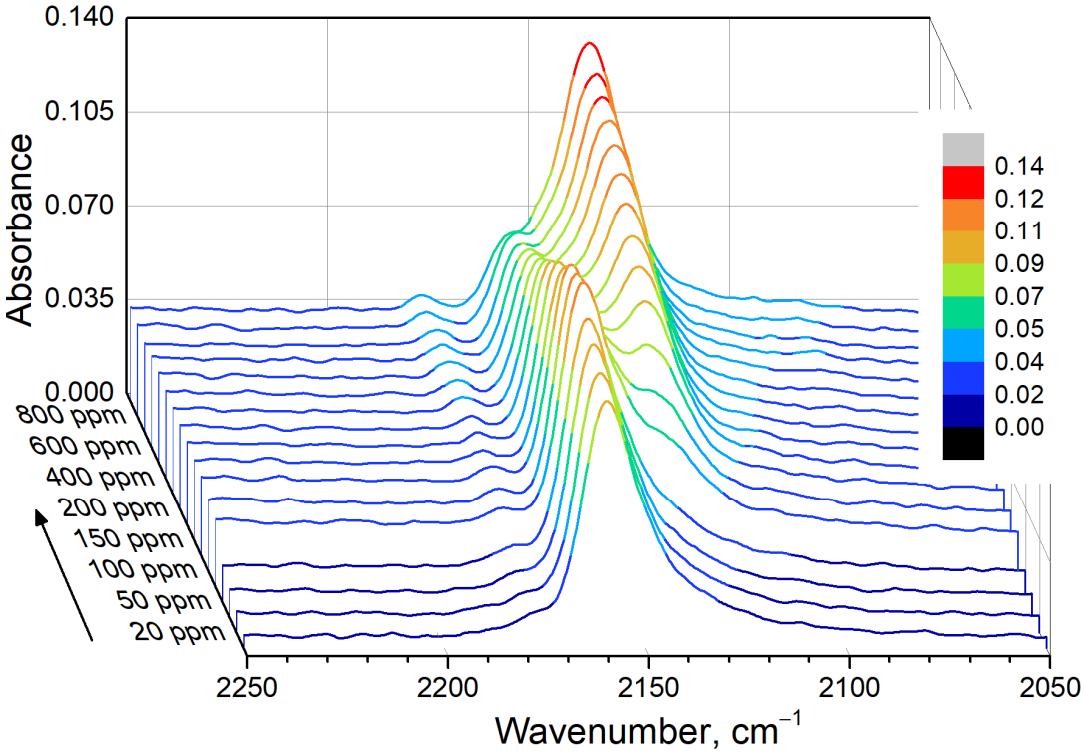

(**A**)

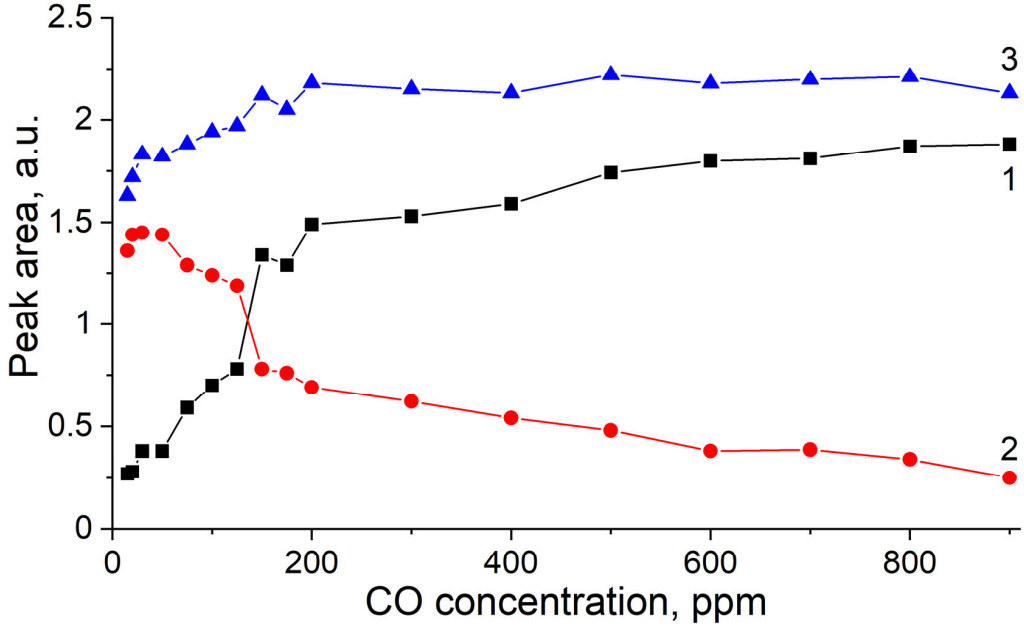

(**B**)

Figure 6. (**A**) Waterfall graph of difference FTIR spectra of CO adsorbed on MOR-Cu$(NO_3)_2$ in Ar flow. For all waterfall data sets, the spectra are offset for clarity, and the colour legend represents the absorbance scale. (**B**) Evolution of the peak areas: 2135 cm^{-1} peak (1), 2157 cm^{-1} peak (2) and total peak area (3) of CO adsorbed on Cu$(NO_3)_2$-MOR.

3.6. In Vacuo CO–H_2O Coadsorption on $Cu(NO_3)_2$-MOR

The effect of water vapour on CO adsorption was further studied using the vacuum cell setup. The concentration of CO was recalculated based on the partial pressure of CO to allow for a comparison between the two sets of experiments, e.g., 0.05 mbar of CO introduced to the vacuum cell would correspond to 50 ppm in the flow system (see Figures 7A,B and S10, step A). Subsequently, water was added in 0.1 µL portions (5.55 µmol, ~150 ppm) to monitor the transition of the peak at 2157 cm^{-1} to 2135 cm^{-1} (step B). The complete transition was observed after the addition of 0.6 µL of H_2O. To confirm that the shift was reversible, the sample was evacuated for 30 min (step C) and the introduction of 0.6 µL of H_2O was repeated (step D). Figure 7A,B demonstrate that the peak intensities and positions are reproducible. This indicates that in a potential real-life exposure of the sensor, where changes in humidity are frequent, the sensor should keep its functionality.

Additionally, the sensor was first exposed to 1 µL of water (55.5 µmol, ~1500 ppm) (step A), followed by CO adsorption (50 to 1000 ppm) (step B). At the lower CO concentrations, the peak intensity was significantly lower than on a dry sample (Figures S11 and S12). However, after the sample was exposed to CO concentrations that were comparable to the initial water concentration, the peak shapes and intensities were regained. The evacuation experiment demonstrated that the water adsorption was reversible (step C).

Even though the total area of the peaks, which would be detected by an NDIR-type sensor, was not affected during the in situ and vacuum experiments, the CO detection sensor was significantly more sensitive in the absence of water. Therefore, a more suitable sensor material, based on zeolite BEA-19, was utilised. This material was less hydrophilic and showed promising results during the initial screening (Table 3).

3.7. Cu-Impregnated Sn-BEA

The hydrophobic Sn-BEA zeolite was chosen due to its well-known synthesis procedure [19,30], and BEA-19 was used as a starting material. Hydrophobicity of the material was accomplished by fluoride-assisted synthesis, during which the silanols initially present on the zeolite surface were replaced by fluoride groups [19,30]. $Cu(NO_3)_2$-impregnated Sn-BEA (CuSn-BEA) was characterised by using XRD to confirm that the prepared material had the BEA framework and the basic copper salt was impregnated (Figure 8A). A more detailed characterisation of hydrophobic Sn-BEA and its application as a selective NO_2 sensor was presented in one of our previous publications [31]. The TGA curves for the obtained Sn-BEA and MOR zeolites are shown in Figure 8B. MOR contains almost 10 wt% of water, which could block the microporous channels and interfere with CO adsorption on copper sites. On the other hand, the weight loss due to water in Sn-BEA is ~1 wt%. Therefore, it is expected that such a hydrophobic sample should perform better under environmental conditions with relatively high humidity levels.

3.8. CO–H_2O Co-Adsorption on CuSn-BEA

CO adsorption on CuSn-BEA was examined using in situ experiments in an Ar flow containing 100 ppm of water vapour (Figures 9A,B and S13). The two main bands observed at 2149 cm^{-1} (narrow) and 2132 cm^{-1} (broad) can be attributed to the Cu^+-CO and Cu^+-$(CO)_2$ species, respectively. At concentrations greater than 400 ppm of CO in the flow, the 2149 cm^{-1} peak area remained at a stable value, indicating the saturation of the Cu^+-CO species. However, the sensor was still able to discriminate the higher CO concentrations due to an increase in the area of the 2132 cm^{-1} band. The 100 ppm of water vapour present in the test gases did not affect the peak positions in CuSn-BEA; therefore, this zeolite appears to be a more promising material for the proposed sensor. Furthermore, the total peak areas, and therefore the sensor sensitivity, followed a trend similar to that observed for MOR-$Cu(NO_3)_2$ (Figures 6B and 9B).

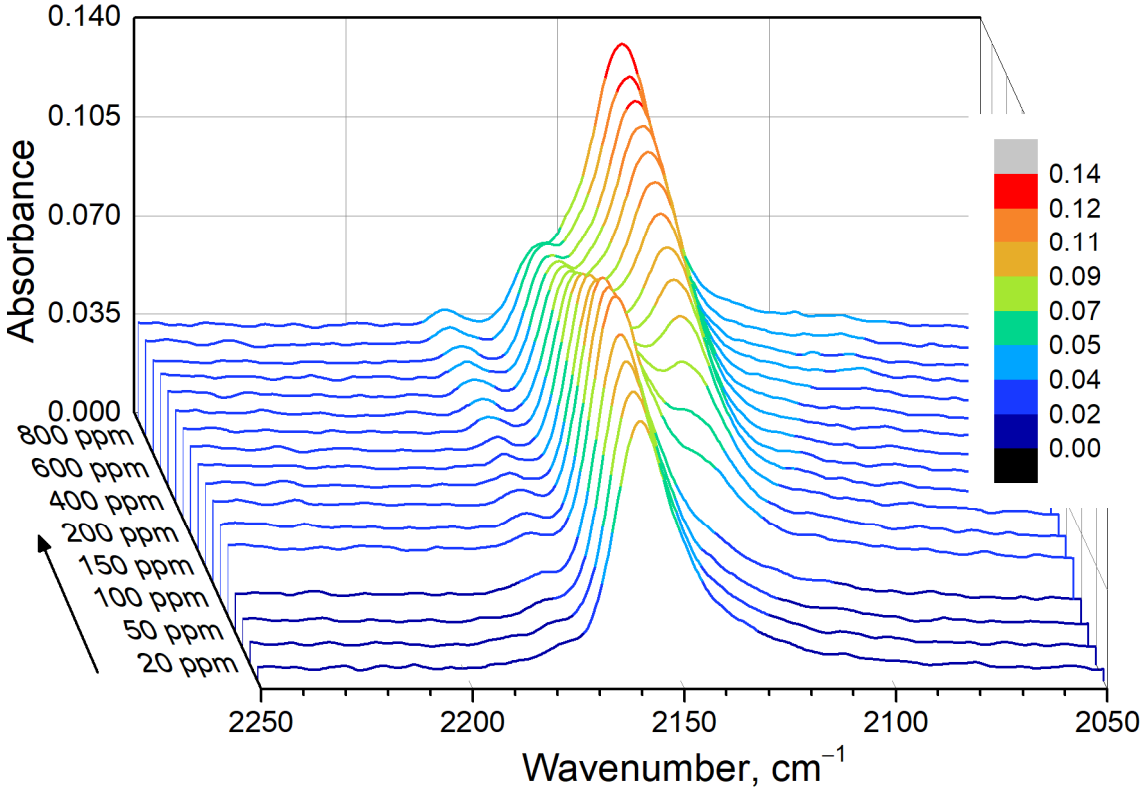

(**A**)

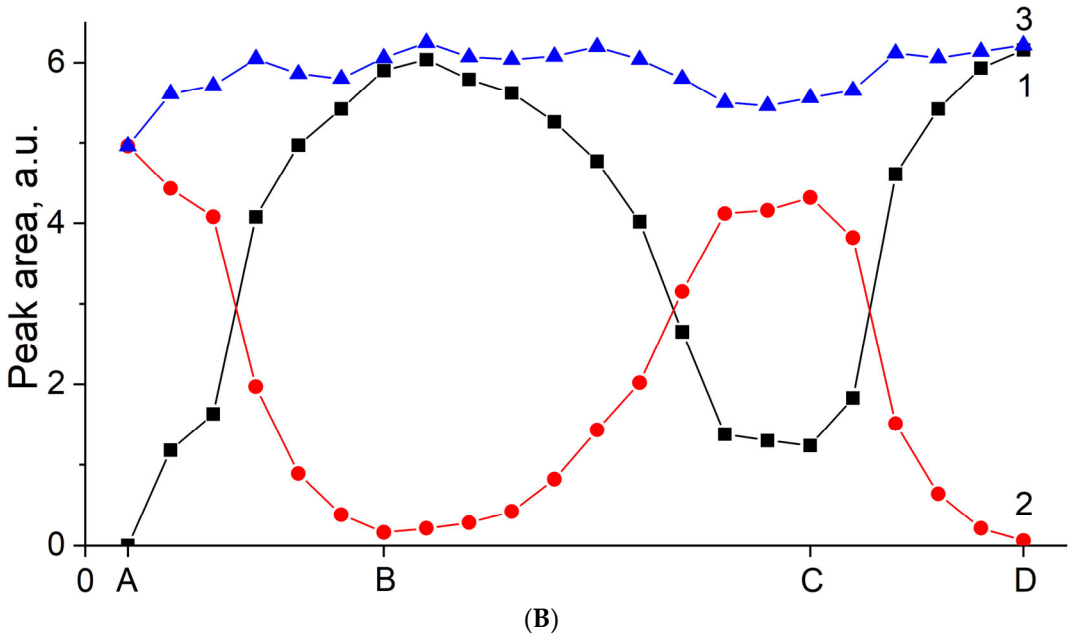

(**B**)

Figure 7. (**A**). Waterfall graph of difference FTIR spectra of CO adsorbed on $Cu(NO_3)_2$-MOR: 50 ppm of CO adsorbed (step A) followed by stepwise H_2O adsorption (step B), evacuation (step C) and H_2O re-adsorption (step D). (**B**) Peak evolution of CO adsorbed on MOR-$Cu(NO_3)_2$ during water adsorption-desorption experiment; 2135 cm^{-1} peak (1), 2157 cm^{-1} peak (2) and total peak area (3); 50 ppm of CO adsorbed (step A) followed by stepwise H_2O adsorption (step B), evacuation (step C) and H_2O re-adsorption (step D).

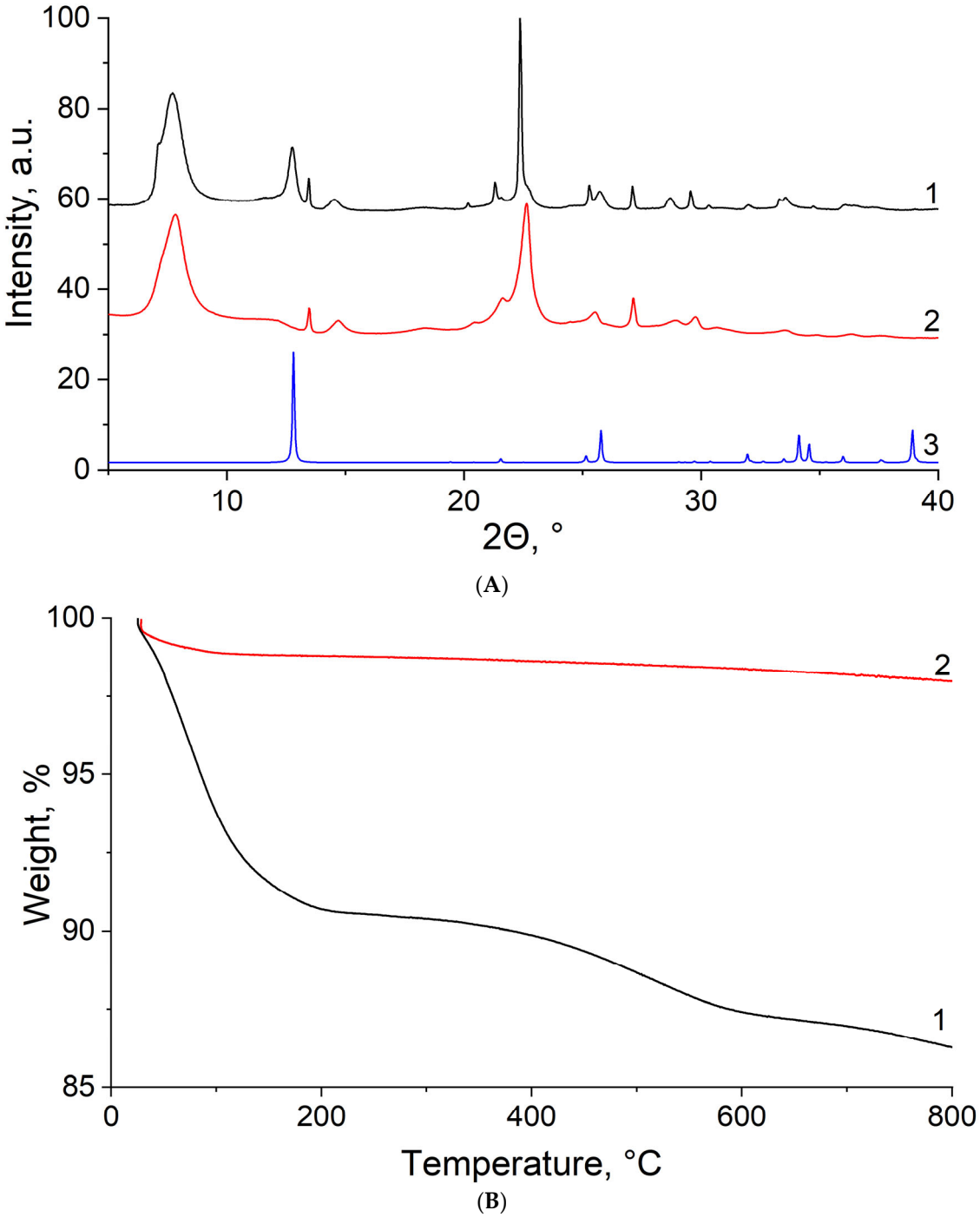

Figure 8. (**A**) XRD patterns of CuSn-BEA (1), BEA-19 (2) and calculated $Cu_2(NO_3)(OH)_3$ (3); patterns are offset for clarity. (**B**) TGA curves of MOR (1) and Sn-BEA (2).

To determine the amount of water required to interfere with the CO adsorption, CuSn-BEA was also subjected to water interference experiments under controlled static conditions in a vacuum system. The data showed that the total CO peak area (2170–2110 cm^{-1}) remained largely unchanged, although there was a reversible intensity redistribution upon adsorption-desorption of water (see Figures S14–S16 and additional details in SI). For instance, in experiments where the H_2O concentration was equivalent to ~1500 ppm and that of CO varied from 10 to 5000 ppm (Figures 10A,B and S17), the sensor response was comparable to the experiment with 100 ppm of water in the flow system. The total peak area evolution followed a similar trend, and the 2149 cm^{-1} peak area reached a plateau

at ~400 ppm. Although there was a significant difference in the 2149 to 2132 cm^{-1} peak area ratio, it did not affect the overall trend and should not present a problem for the performance of the proposed sensor in an NDIR setup as the water vapour did not interfere with the peak evolution. These data demonstrate that CuSn-BEA could be the optimum material among the studied zeolite samples for the intended environmental CO sensor.

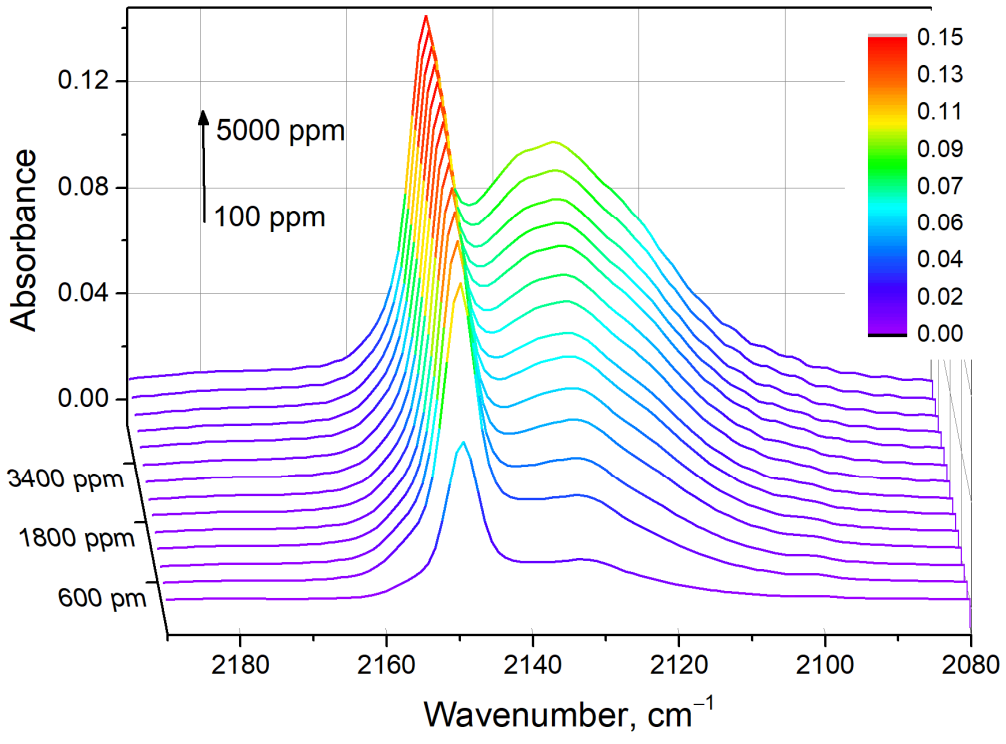

(**A**)

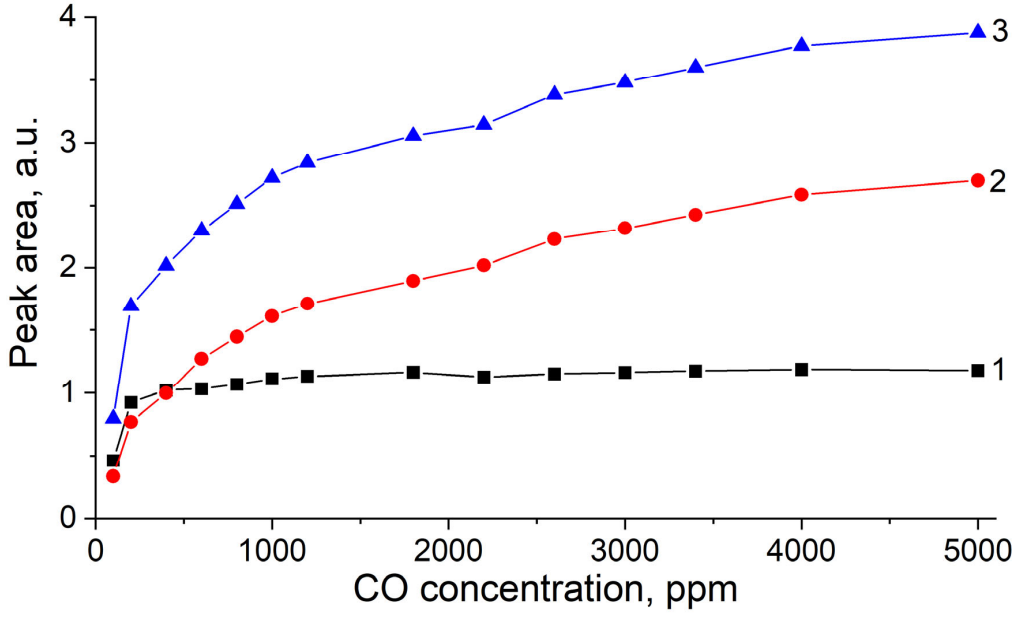

(**B**)

Figure 9. (**A**) Difference FTIR spectra of CO adsorbed on CuSn-BEA; 100–5000 ppm (in Ar flow containing 100 ppm of water vapour). (**B**) Evolution of the total peak area of CO adsorbed on CuSn-BEA; 100–5000 ppm; 2149 cm^{-1} peak (1), 2132 cm^{-1} peak (2) and total peak area (3).

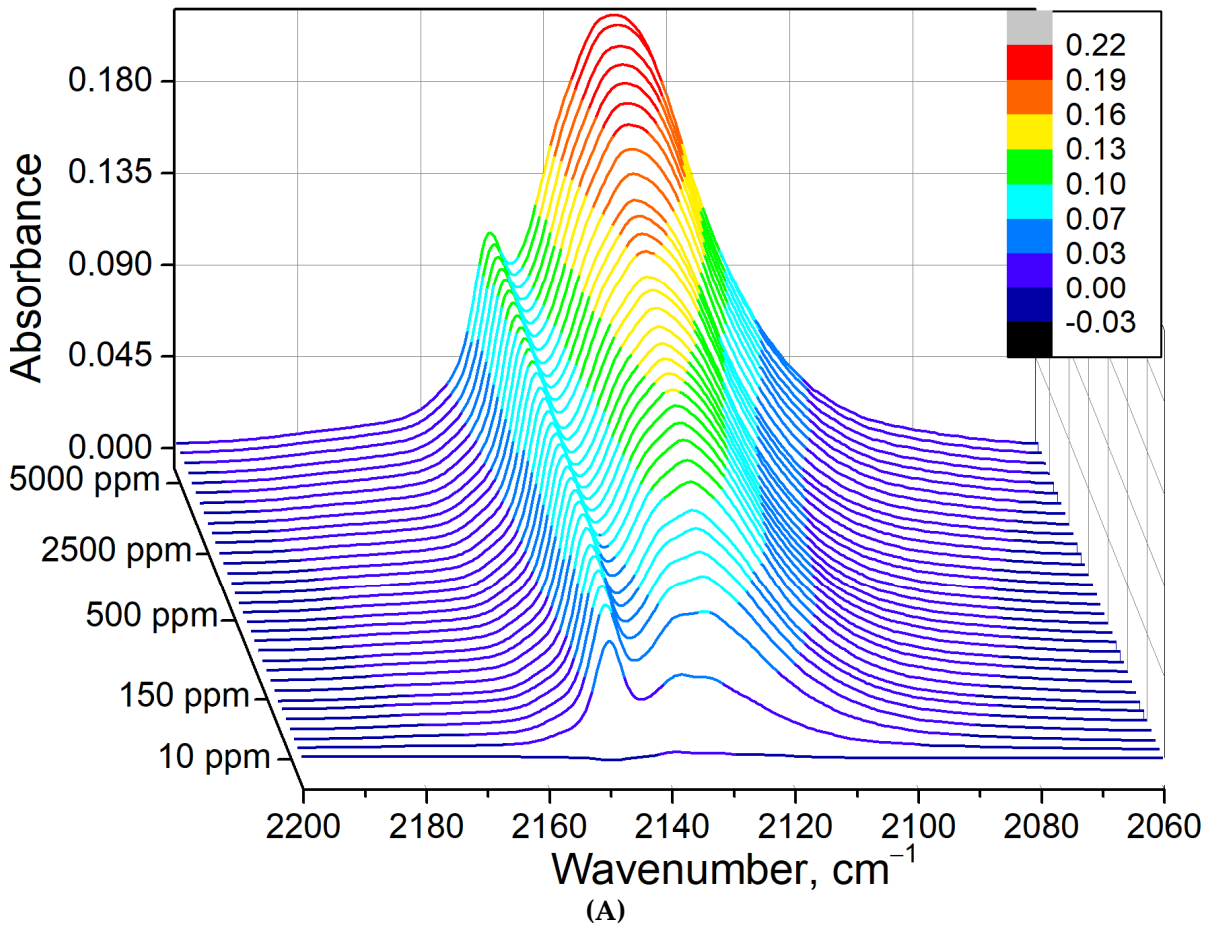

(A)

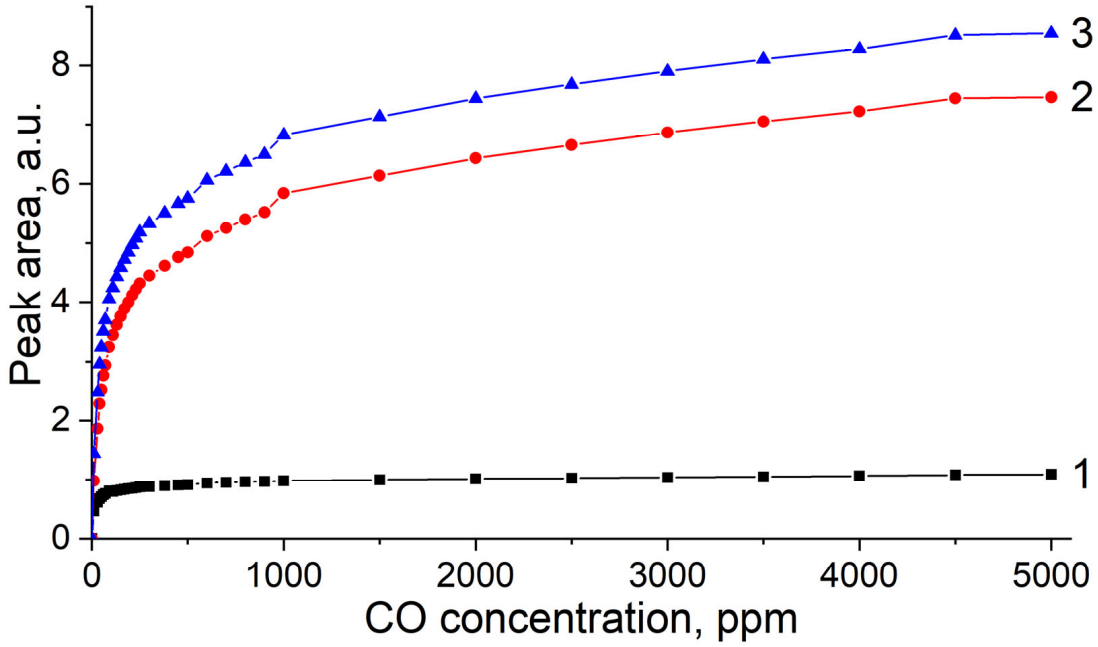

(B)

Figure 10. (**A**) Waterfall graph of difference FTIR spectra of CuSn-BEA in vacuo after saturation with ~1500 ppm of H_2O followed by CO adsorption; 10 to 5000 ppm. (**B**) Evolution of the total peak area of CO adsorbed on CuSn-BEA in the humid environment (1500 ppm of H_2O); 10–5000 ppm; 2149 cm^{-1} peak (1), 2132 cm^{-1} peak (2) and total peak area (3).

4. Conclusions

This work demonstrates the potential of Cu-containing zeolites as the sensing element for infrared detection of carbon monoxide. Since Cu^+ forms stable complexes with CO at room temperature, which can be observed by IR spectroscopy, a range of commercial samples (NaX, NaY, MOR, FER, BEA-12, BEA-19 and ZSM-5) were ion-exchanged or impregnated using $CuSO_4$, $Cu(NO_3)_2$ and $Cu(OAc)_2$ as copper sources to prepare Cu^+-containing zeolites. Following its activation, $Cu(NO_3)_2$-impregnated MOR showed the highest concentration of Cu^+ species. Both titration experiments and tests carried out under environmental and in situ flow conditions confirmed the high sensitivity of MOR-$Cu(NO_3)_2$ as a potential CO sensor. However, its excellent performance can be compromised by water adsorption. To counter significant water interference, $Cu(NO_3)_2$-impregnated hydrophobic Sn-BEA was prepared and evaluated under representative testing conditions. The Cu^+-containing zeolites successfully demonstrated the ability to discriminate CO concentrations from 10 to 5000 ppm at room temperature. Additionally, these zeolite-based sensors were operational at environmental levels of humidity. To the best of our knowledge, this is the first report on Cu-modified zeolites utilised as CO sensors, which provides a basis for testing zeolites modified by other transition metals for gas sensing applications. However, further optimisation is required for these materials to be competitive against the sensors currently available on the market. Response selectivity, reproducibility and repeatability need to be evaluated, and the water interference effects must be calibrated. In particular, since the typical operational time of competing sensors is 5–10 years, the issues related to the lifespan and regeneration of the proposed sensors must be carefully addressed.

Supplementary Materials: The following supporting information can be downloaded at: https://www.mdpi.com/article/10.3390/chemistry5010024/s1, Figure S1: FTIR spectrometer and vacuum cell; Figure S2: Calculated (1) and experimental (2) XRD patterns of $Cu_2(NO_3)(OH)_3$ (a), $CuSO_4 \cdot 3Cu(OH)_2$ (b) and $[Cu(OAc)_2]_2 \cdot Cu(OH)_2 \cdot 5H2O$ (c); calculated patterns are simulated from the structures deposited in ICSD and ICDD; Figure S3: XRD patterns of MOR $Cu(NO_3)_2$ before activation (1), MOR $Cu(NO_3)_2$ after activation (2), the calculated pattern of $Cu_2(NO_3)(OH)_3$ (3), the calculated pattern of CuO (4), the calculated pattern of Cu_2O (5) patterns are offset and calculated patterns are scaled for clarity; Figure S4: FTIR spectra of CO adsorbed on $Cu(NO_3)_2$-impregnated fumed silica (1) and 5000 ppm of CO* (2), * spectrum is offset and multiplied by 5 for clarity; Figure S5: Difference FTIR spectra of CO adsorbed on MOR ion-exchanged (one) and impregnated (two) by $Cu(NO_3)_2$ solution; Figure S6: Difference FTIR spectra of CO adsorbed on BEA-12 impregnated with $CuSO_4$ (1), $Cu(NO_3)_2$ (2), $Cu(OAc)_2$ (3), spectra are offset for clarity; Figure S7: Time-dependent evolution of the IR peak area following CO adsorption on MOR-Cu(NO3)2 (black) and evolution of IR peak area during stepwise desorption at different temperatures of CO on MOR-$Cu(NO_3)_2$ (red); Figure S8: Difference FTIR spectra of $Cu(NO_3)_2$-impregnated MOR: exposed to air for 5 min (1), exposed to CO in the air for 2 min (2); Figure S9: Waterfall graph of difference FTIR spectra of CO adsorbed on CuMOR in Ar flow. For all waterfall sets of spectra, they are offset for clarity and the colour legend represents the absorbance scale; Figure S10: Waterfall graph of difference FTIR spectra of CO adsorbed on $Cu(NO_3)_2$-impregnated MOR, 50 ppm of CO adsorbed (step A) followed by stepwise H_2O adsorption (step B), evacuation (step C) and H2O re-adsorption (step D); Figure S11: Waterfall graph of difference FTIR spectra of CO adsorbed on $Cu(NO_3)_2$-impregnated MOR after 1 µL H_2O adsorption (step A), followed by CO introduction at different partial pressures (50–1000 ppm) (step B) and evacuation (step C); Figure S12: Waterfall graph of difference FTIR spectra of CO adsorbed on $Cu(NO_3)_2$-MOR after 1 µL H_2O adsorption (step A), followed by CO introduction at different partial pressures (50–1000 ppm) (step B) and evacuation (step C); Figure S13: Difference FTIR spectra of CO adsorbed on CuSn-BEA, 100–5000 ppm (in Ar flow containing 100 ppm of water vapour); Figure S14: Waterfall graph of difference FTIR spectra of CO adsorbed on CuSn-BEA (step A), water interference experiment (step B) and desorption experiment (step C) and water readsorption (step D); Figure S15: 2D contour map of difference FTIR spectra of CO adsorbed on CuSn-BEA (step A), water interference experiment (step B) and desorption experiment (step C) and water re-adsorption (step D), colour legend represents the absorbance scale; Figure S16: Waterfall graph of difference FTIR spectra of CO adsorbed on CuSn-BEA (step A), water interference experiment (step B) and desorption experiment (step C) and water readsorption (step D); Figure S17: Waterfall graph of difference FTIR spectra of CuSn-BEA in vacuo

after saturation with ~1500 ppm of H2O followed by CO adsorption, 10 to 5000 ppm; Table S1: Zeolite properties of the zeolites used in this work, Si/Al values were determined by the manufacturers, MR—membered ring; Figure S18–S46, Table S2: Supplementary Characterisation File.

Author Contributions: Conceptualisation, M.J., J.G., L.L., S.M. and V.Z.; Methodology, M.J., J.G., L.L., P.B. and V.Z.; Formal Analysis, M.J. and V.Z.; Investigation, M.J.; Resources, S.M. and V.Z.; Data Curation, M.J.; Writing—Original Draft Preparation, M.J.; Writing—Review and Editing, L.L., S.M. and V.Z.; Visualization, M.J.; Supervision, J.G., L.L., P.B., S.M. and V.Z.; Project Administration, S.M. and V.Z.; Funding Acquisition, S.M. and V.Z. All authors have read and agreed to the published version of the manuscript.

Funding: M.J.'s PhD has been funded by the Royal Society (IE160562), Keele University (KU-T6316), and the Newton Fund (Grant #261867079).

Institutional Review Board Statement: Not applicable.

Informed Consent Statement: Not applicable.

Data Availability Statement: https://researchdata.keele.ac.uk/.

Acknowledgments: S.M. and L.L. would like to thank the Centre of Nanozeolites and Related Porous Materials, Région Normandie, CNRS (CLEAR), for supporting this work. M.J. would like to thank the Royal Society, Keele University, and the Newton Fund for funding his PhD project, as well as the staff of Keele University and Normandie Université-ENSICAEN for the help provided during the project.

Conflicts of Interest: The authors declare no conflict of interest.

References

1. Cobb, N.; Etzel, R.A. Unintentional Carbon Monoxide—Related Deaths in the United States, 1979 Through 1988. *JAMA* **1991**, *266*, 659–663. [CrossRef] [PubMed]
2. Goldstein, M. Carbon Monoxide Poisoning. *J. Emerg. Nurs.* **2008**, *34*, 538–542. [CrossRef] [PubMed]
3. Struttmann, T.; Scheerer, A.; Scott Prince, T.; Goldstein, L. Unintentional Carbon Monoxide Poisoning From an Unlikely Source. *J. Am. Board Fam. Pract.* **1998**, *11*, 481–484. [CrossRef] [PubMed]
4. Fine, G.F.; Cavanagh, L.M.; Afonja, A.; Binions, R. Metal Oxide Semi-Conductor Gas Sensors in Environmental Monitoring. *Sensors* **2010**, *10*, 5469–5502. [CrossRef] [PubMed]
5. Nandy, T.; Coutu, R.A.; Ababei, C. Carbon monoxide sensing technologies for next-generation cyber-physical systems. *Sensors* **2018**, *18*, 3443. [CrossRef]
6. Kosterev, A.A.; Bakhirkin, Y.A.; Tittel, F.K. Ultrasensitive gas detection by quartz-enhanced photoacoustic spectroscopy in the fundamental molecular absorption bands region. *Appl. Phys. B Lasers Opt.* **2005**, *80*, 133–138. [CrossRef]
7. Li, L.; Cao, F.; Wang, Y.; Cong, M.; Li, L.; An, Y.; Song, Z.; Guo, S.; Liu, F.; Wang, L. Design and characteristics of quantum cascade laser-based CO detection system. *Sens. Actuators B Chem.* **2009**, *142*, 33–38. [CrossRef]
8. Wiegleb, G.; Heitbaum, J. Semiconductor gas sensor for detecting NO and CO traces in ambient air of road traffic. *Sens. Actuators B Chem.* **1994**, *17*, 93–99. [CrossRef]
9. *Carbon Monoxide Detector Market—Forecasts from 2021 to 2026*; Research and Markets: Dublin, Ireland, 2021.
10. Mahajan, S.; Jagtap, S. Metal-oxide semiconductors for carbon monoxide (CO) gas sensing: A review. *Appl. Mater. Today* **2020**, *18*, 100483. [CrossRef]
11. Basu, A.K.; Chauhan, P.S.; Awasthi, M.; Bhattacharya, S. α-Fe_2O_3 loaded rGO nanosheets based fast response/recovery CO gas sensor at room temperature. *Appl. Surf. Sci.* **2019**, *465*, 56–66. [CrossRef]
12. Zhang, D.; Wu, J.; Cao, Y. Cobalt-doped indium oxide/molybdenum disulfide ternary nanocomposite toward carbon monoxide gas sensing. *J. Alloys Compd.* **2019**, *777*, 443–453. [CrossRef]
13. *Introduction to Zeolite Science and Practice*; Cejka, J.; van Bekkum, H.; Corma, A.; Schuth, F. (Eds.) Elsevier Science: Amsterdam, The Netherlands, 2007.
14. Bordiga, S.; Lamberti, C.; Bonino, F.; Travert, A.; Thibault-Starzyk, F. Probing zeolites by vibrational spectroscopies chemical society reviews probing zeolites by vibrational spectroscopies. *Chem. Soc. Rev.* **2015**, *44*, 7262–7341. [CrossRef] [PubMed]
15. Hadjiivanov, K.I.; Vayssilov, G.N. Characterization of oxide surfaces and zeolites by carbon monoxide as an IR probe molecule. *Adv. Catal.* **2002**, *47*, 307–511.
16. Nachtigallová, D.; Bludský, O.; Otero Aerán, C.; Bulánek, R.; Nachtigall, P. The vibrational dynamics of carbon monoxide in a confined space-CO in zeolites. *Phys. Chem. Chem. Phys* **2006**, *8*, 4849–4852. [CrossRef]
17. Kharchenko, A.; Zholobenko, V.; Vicente, A.; Fernandez, C.; Vezin, H.; De Waele, V.; Mintova, S. Formation of copper nanoparticles in LTL nanosized zeolite: Spectroscopic characterization. *Phys. Chem. Chem. Phys.* **2018**, *20*, 2880–2889. [CrossRef] [PubMed]

18. Spoto, G.; Zecchina, A.; Bordiga, S.; Ricchiardi, G.; Martra, G.; Leofanti, G.; Petrini, G. Cu (I)-ZSM-5 zeolites prepared by reaction of H-ZSM-5 with gaseous CuCl: Spectroscopic characterization and reactivity towards carbon monoxide and nitric oxide. *Appl. Catal. B Environ.* **1994**, *3*, 151–172. [CrossRef]
19. Harris, J.W.; Cordon, M.J.; Di Iorio, J.R.; Vega-Vila, J.C.; Ribeiro, F.H.; Gounder, R. Titration and quantification of open and closed Lewis acid sites in Sn-Beta zeolites that catalyze glucose isomerization. *J. Catal.* **2016**, *335*, 141–154. [CrossRef]
20. Kobler, J.; Abrevaya, H.; Mintova, S.; Bein, T. High-Silica Zeolite-: From Stable Colloidal Suspensions to Thin Films. *J. Phys. Chem. C* **2008**, *112*, 14274–14280. [CrossRef]
21. Al-Ani, A.; Haslam, J.J.C.; Mordvinova, N.E.; Lebedev, O.I.; Vicente, A.; Fernandez, C.; Zholobenko, V. Synthesis of nanostructured catalysts by surfactantlating of large-pore zeolites. *Nanoscale Adv.* **2019**, *1*, 2029–2039. [CrossRef]
22. Baerlocher, C.; Mccusker, L.B.; Olson, D.H. *Atlas of Zeolite Framework Types*; Elsevier: Amsterdam, The Netherlands, 2007.
23. Bordiga, S.; Lamberti, C.; Geobaldo, F.; Zecchina, A.; Palomino, G.T.; Areán, C.O. Fourier-Transform Infrared Study of CO Adsorbed at 77 K on H-Mordenite and Alkali-Metal-Exchanged Mordenites. *Langmuir* **1995**, *11*, 527–533. [CrossRef]
24. Palomino, G.T.; Zecchina, A.; Giamello, E.; Fisicaro, P.; Berlier, G.; Lamberti, C.; Bordiga, S. Polycarbonylic and polynitrosylic species in Cu I-exchanged ZSM-5, β, Mordenite and Y zeolites: Comparison with homogeneous complexes. *Stud. Surf. Sci. Catal.* **2000**, *130*, 2915–2920.
25. Lamberti, C.; Bordiga, S.; Zecchina, A.; Salvalaggio, M.; Geobaldoc, F.; Otero, C. XANES, EXAFS and FTIR characterization of copper-exchanged mordenite. *J. Chem. Soc. Faraday Trans.* **1998**, *94*, 1519–1525. [CrossRef]
26. Turnes Palomino, G.; Bordiga, S.; Lamberti, C.; Zecchina, A.; Otero Areán, C. Vibrational and optical spectroscopic studies on copper-exchanged ferrierite. *Stud. Surf. Sci. Catal.* **2002**, *1142*, 199–206.
27. Giordanino, F.; Vennestrøm, P.N.R.; Lundegaard, L.F.; Stappen, F.N.; Mossin, S.; Beato, P.; Bordiga, S.; Lamberti, C. Characterization of Cu-exchanged SSZ-13: A comparative FTIR, UV-Vis, and EPR study with Cu-ZSM-5 and Cu-β with similar Si/Al and Cu/Al ratios. *Dalt. Trans* **2013**, *42*, 12741. [CrossRef]
28. Lamberti, C.; Bordiga, S.; Salvalaggio, M.; Spoto, G.; Zecchina, A.; Geobaldo, F.; Vlaic, G.; Bellatreccia, M. XAFS, IR, and UV−Vis Study of the CuI Environment in CuI-ZSM-5. *J. Phys. Chem. B* **1997**, *101*, 344–360. [CrossRef]
29. Zholobenko, V.; Freitas, C.; Jendrlin, M.; Bazin, P.; Travert, A.; Thibault-Starzyk, F. Probing the acid sites of zeolites with pyridine: Quantitative AGIR measurements of the molar absorption coefficients. *J. Catal.* **2020**, *385*, 52–60. [CrossRef]
30. Corma, A.; Nemeth, L.T.; Renz, M.; Valencia, S. Sn-zeolite beta as a heterogeneous chemoselective catalyst for Baeyer-Villiger oxidations. *Nature* **2001**, *412*, 423–425. [CrossRef]
31. Jendrlin, M.; Grand, J.; Lakiss, L.; Dubray, F.; Bazin, P.; El Fallah, J.; Mintova, S.; Zholobenko, V. Environmental applications of zeolites: Hydrophobic Sn-BEA as a selective gas sensor for exhaust fumes. *Submitt. Chem.* **2023**.